Physics of the Earth and Planetary Interiors 241 (2015) 1–14

Contents lists available at ScienceDirect

Physics of the Earth and Planetary Interiors

journal homepage: www.elsevier.com/locate/pepi

Crustal structure of the North Anatolian and East Anatolian Fault Systems from magnetotelluric data

Erşan Türkoğlu [a], Martyn Unsworth [a,*], Fatih Bulut [b], İlyas Çağlar [c]

[a] Department of Physics, University of Alberta, Edmonton, AB T6G 2G7, Canada
[b] Istanbul Aydın University AFAM Disaster Research Centre, Inonu Cad. 38, 34295 Istanbul, Turkey
[c] Department of Geophysical Engineering, Faculty of Mines, Istanbul Technical University, Maslak, Istanbul 34469, Turkey

ARTICLE INFO

Article history:
Received 28 March 2014
Received in revised form 20 December 2014
Accepted 9 January 2015
Available online 30 January 2015

Keywords:
Magnetotellurics
Resistivity
Fault zone conductor
Eastern Anatolia
North Anatolian Fault
East Anatolian Fault

ABSTRACT

Magnetotelluric (MT) studies can map subsurface resistivity structure and have located zones of low resistivity (high conductivity) within major strike-slip fault zones worldwide which have been interpreted as regions of elevated fluid content. This study describes MT data from the eastern part of the North Anatolian and the East Anatolian Fault Systems (NAFS and EAFS) and presents the results of the first MT studies of these faults. The inversion of the MT data produced 2-D resistivity models which showed that both fault systems are underlain by a broad low resistivity zone that extended into the lower crust. However, the resistivity beneath the East Anatolian Fault System was much lower than beneath the eastern part of the North Anatolian Fault System. These conductors begin at a depth of 10 km – not at the surface as on the central San Andreas Fault (SAFS). This difference is interpreted as being due to the fact that the EAFS and NAFS are young fault systems characterized in the upper crust by multiple fault traces – as opposed to the SAFS that has evolved into a single through going fault. Different stages of the seismic cycle may also influence the resistivity structure, although this is difficult to constrain without knowledge of time variations in resistivity structure at each location.

1. Introduction

Transform faults represent one of the three classes of plate boundaries and pose a significant seismic hazard, as evidenced by recent earthquakes on the North Anatolian, San Andreas, and other faults (Barka and Kadinsky-Cade, 1988; Fuenzalida et al., 1997; Barka et al., 2002; Toppozada and Branum, 2002). Strike-slip faults exhibit a wide variability in their seismogenic behavior. Some faults are characterized by segments that exhibit continuous creep, with adjacent segments locked and rupturing during major earthquakes. The physical cause of these variations in behavior is not well understood. The structure of strike-slip faults in the ductile lower crust is also an ongoing research question (Becken et al., 2008). Geological studies of exhumed faults and shear zones suggest that the zone of deformation broadens with depth (Sibson, 1977; Hanmer, 1988). Geophysical studies of the lower crust beneath shear zones are limited in number, but indicate that fluid composition is an important parameter that may influence the style of deformation (Bedrosian et al., 2004). Deformation in the ductile lower crust is influenced by fluids and laboratory studies suggest that deformation in the ductile part of the crust may occur by creep processes that are enhanced by the presence of water (Tullis et al., 1996). It has also been proposed that in the brittle upper crust, the behavior of seismogenic faults may be controlled by spatial and temporal variations in fluid content (Byerlee, 1993; Sleep and Blanpied, 1992). Over-pressured fluids in the fault-zone may trigger earthquakes through reducing the effective normal stress and thereby lowering the shear stress needed for failure (Sleep and Blanpied, 1992). A related observation is that strike-slip faults are often observed to be mechanically weak. For example, the San Andreas Fault System (SAFS) appears to move with a shear stress of just 10–20 MPa, that corresponds to a coefficient of friction in the range 0.1–0.2 (Zoback et al., 1987; Mount and Suppe, 1987). Similar values (0.05–0.2) have been reported on the NAFS based on geodetic data (Provost et al., 2003). These frictional values are significantly lower than those obtained in laboratory studies of rock friction (Byerlee, 1978; Sibson, 1974) and are consistent with the low values of frictional heat generation reported from the San Andreas Fault by Williams et al. (2004).

A key question that arises in this debate is how the amount of fluid and type of deformation are related in strike-slip faults. It is possible that either (a) an increase in the amount of fluid causes a fault to weaken and rupture, or (b) that the amount of fluid is

* Corresponding author. Tel.: +1 780 492 3041.
E-mail address: Unsworth@UAlberta.ca (M. Unsworth).

http://dx.doi.org/10.1016/j.pepi.2015.01.003
0031-9201/

the result of elevated porosity caused by deformation. This question can be addressed by mapping the subsurface distribution of fluids within major strike-slip faults using surface based geophysical studies. Electromagnetic (EM) methods are effective in this regard because they image subsurface resistivity – a rock property that is largely controlled in the upper crust by the amount, salinity and geometry of the pore fluids. In this context, magnetotellurics (MT) is the most useful because it can image the entire crust using natural EM signals, without the need for a transmitter. Depth sounding in MT is achieved through the skin-depth phenomenon that gives a penetration depth that is inversely related to the signal frequency (Vozoff, 1991).

A number of MT surveys have been used to study the fluid distribution within active strike-slip fault zones. Studies of the San Andreas Fault (SAF) in California revealed that some fault segments are characterized by a zone of low resistivity (elevated conductivity). At Parkfield, the SAF is in transition from creeping to locked and the conductor extends from the surface to a depth of 2–3 km (Unsworth et al., 1997). The conductor extends to mid-crustal depths at Hollister where the fault creeps at 10–15 mm/yr (Burford and Harsh, 1980; Evans et al., 1981; Bedrosian et al., 2002). A small fault-zone conductor was observed on the locked Carrizo segment (Unsworth et al., 1999; Mackie et al., 1997). Deeper fault zone structure of the SAF was investigated with the longer profile and 3-D array of Becken et al. (2008) and showed a continuous zone of low resistivity extending through the entire crust.

In northwest Turkey, a number of MT studies have investigated the resistivity structure of the North Anatolian Fault close to the ruptures of the İzmit and Düzce earthquakes and revealed deeper zones of low resistivity in the mid-crust (Tank et al., 2005; Kaya et al., 2009). More recent studies have used seafloor MT to study the fault strand of the NAF under the Sea of Marmara (Kaya et al., 2013). In China, a number of MT studies have investigated the Kunlun and Altyn Tagh Faults which are major strike-slip faults associated with the northern margin of India–Asia collision (Unsworth et al., 2004; Le Pape et al., 2012; Zhang et al., 2015). Bai et al. (2010) described major conductors in the mid-crust that were coincident with major shear zones in southwest China over horizontal distances of hundreds of kilometers. The Alpine Fault in New Zealand was studied with MT by Wannamaker et al. (2002). These studies have detected conductors in two distinct tectonic environments. To make a clear distinction between these, separate abbreviations are used in this paper:

(1) Shallow conductors associated with the damage zone of a fault, and caused by groundwater present in regions of elevated porosity, and perhaps supplemented with clay mineralization. These are termed damage zone conductors (DZC).
(2) Deeper conductors in the mid-crust, generally extending across the brittle–ductile transition are called crustal fault-zone conductors (CFZC).

The object of this paper is to present new images of the electrical resistivity structure of the major strike-slip faults in Eastern Anatolia, with the goal of being able to relate the electrical resistivity structure to the style of deformation. The NAFS and EAFS are relatively young strike-slip faults that have relatively small offsets and have not yet developed into mature strike-slip fault zones. Studying faults at an early stage of development allows the opportunity to address the question of how the structure of fault zones evolves over time.

2. Tectonic setting and previous studies

The tectonics of Eastern Anatolia is dominated by the ongoing collision of the Eurasian and Arabian Plates (Fig. 1). Convergence in the Eocene was initially accommodated by shortening and thickening of the Arabian continental margin (Hempton, 1985; Şengör et al., 1985). The NAFS and EAFS subsequently developed to accommodate the westward motion of the Anatolian block towards the Aegean arc (Burke and Sengör, 1986). Forces generated by trench rollback and the southward migration at the Aegean arc contribute to the westward motion of the Anatolian block along the large-scale strike slip fault systems (Reilinger et al., 2006). Today, the Arabian Plate moves northward at a velocity of 15 mm/yr and only 10% of this convergence is accommodated by lithospheric shortening with the remainder of the convergence accommodated by strike-slip motion on the NAFS and EAFS (Reilinger et al., 2006). Recent studies have shown that the present day driving force for the westward movement of the Anatolian plate is primarily derived from the Aegean subduction, with only a small component

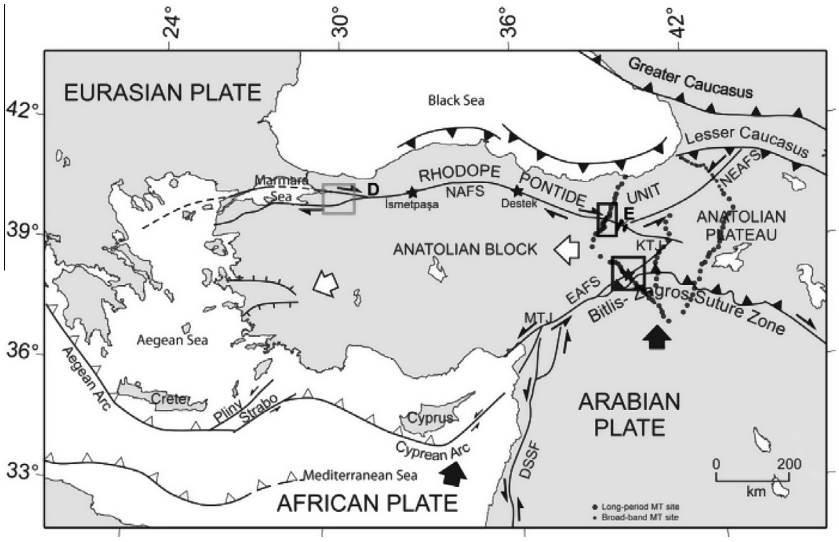

Fig. 1. Simplified tectonic map of Turkey and surroundings (modified from Şengör et al., 1985; Barka, 1992). Black rectangles indicate the areas studied with MT data in this paper. The gray rectangle, east of the Marmara Sea, shows the survey area of Tank et al. (2005). Star symbols show the location of previously reported creep on the NAF and EAF. Filled circles show MT sites (Türkoğlu et al., 2008) NAFS: North Anatolian Fault System. NEAFS: North East Anatolian Fault System. EAFS: East Anatolian Fault System. DSFS: Dead Sea Fault System. KTJ: Karlıova Triple Junction. MTJ: Maraş Triple Junction. D: Düzce. E: Erzincan.

coming from the collision in Eastern Anatolia (Reilinger et al., 2006; Bulut et al., 2012).

2.1. North Anatolian Fault System (NAFS)

Recent seismic activity on the NAFS has been characterized by a sequence of westward propagating earthquakes that began with the M_s = 8.2 Erzincan earthquake in 1939 (Parsons et al., 2000). The most recent earthquakes in this sequence occurred on the western part of the NAFS in 1999 when the August 17 1999 İzmit (M_w = 7.4) and November 12 1999 Düzce (M_w = 7.2) earthquakes ruptured 110–140 km and 40 km of the NAFS, respectively (Armijo et al., 1999; Barka, 1999). Stress modeling by Stein et al. (1997) suggested that these earthquakes have increased the chance of a major earthquake on the strand of the NAFS in the Sea of Marmara (King et al., 2001; Parsons et al., 2000; Le Pichon et al., 2003). Two geodetic studies have identified segments of the NAFS that appear to creep aseismically:

(a) The western NAFS at İsmetpaşa has been monitored for creep since 1957 after major earthquakes in 1944 and 1951 (Çakır et al., 2005; Kutoglu and Akcin, 2006). The creeping motion was reported to be linearly decreasing from ~2 cm/yr in the period 1957–1969 to ~0.8 cm/yr in the period 1992–2002 (Kutoglu and Akcin, 2006). However, it is not clear whether the large earthquakes triggered the creep motion at İsmetpaşa or caused a change in the existing creep rate as there were no measurements before these earthquakes.

(b) Karabacak et al. (2011) used a LIDAR system to study the NAFS in the İsmetpaşa and Destek regions (Fig. 1). Between 2007 and 2009, creep rates at İsmetpaşa were found to be 0.9–1.0 cm/yr which is close to the 0.8 cm/yr reported previously. The aseismic section of NAFS around Destek was also reported to creep at a rate of 0.6–0.7 cm/yr (Karabacak et al., 2011). There are no MT studies at İsmetpaşa or Destek, so it cannot be determined if there is a correlation of electric resistivity structure and seismic behavior, as may be the case for the San Andreas Fault in Central California.

2.2. East Anatolian Fault System (EAFS)

The total offset on the EAFS is around 22 km (Arpat and Şaroğlu, 1972; Şaroğlu et al., 1992), which is less than the 75–85 km observed on the NAFS (Le Pichon et al., 2001). This significant difference could be a consequence of the rollback of the subducting African lithosphere beneath the Aegean arc causing a counterclockwise rotation of the Anatolian block (Reilinger et al., 2006). In contrast to the high levels of seismic activity on the NAFS, the EAFS has been characterized by low seismicity levels during the last century (Jackson and McKenzie, 1988; Ambraseys and Jackson, 1998). However, historical records clearly show that major earthquakes have occurred on this fault in the last 900 years (Ambraseys, 1971; Ambraseys and Jackson, 1998; Nalbant et al., 2002; Taymaz et al., 2007). There is also evidence that seismic activity jumps every 800–900 years from the NAFS to the EAFS and vice versa (Ambraseys, 1971). Continuous broad-band seismograph recordings between October 1999 and August 2001 showed that the EAFS was more active than previously thought and the most active seismogenic zone is at a depth 10–30 km, in contrast to the NAFS where it occurs in the depth range 0–10 km (Turkelli et al., 2003). The more recent study by Bulut et al. (2012) revealed that the EAFS comprises a 20 km wide band of seismicity with complex segmentation with both Riedel and anti-Riedel structures. Precise earthquake locations do not outline a single through-going fault. The focal depths predominantly range between 5 and 20 km. The kinematics are dominated by SW–NE oriented left-lateral strike slip mechanisms reflecting the overall characteristic of the EAFS. The fault zone also contains East–West oriented thrust faults and North–South oriented normal faults. These features may represent an early stage of development of a shear zone, rather than a collisional/or extensional regime (Bulut et al., 2012).

Combined interpretation of magnetic, seismological and geologic data by Dolmaz et al. (2008) showed that a low seismic activity zone on the EAFS coincides with a shallow Curie depth (~14 km) and strong magnetic anomalies (LSZ in Fig. 2). They interpreted this area to have relatively thin crust (36–38 km) and higher crustal temperatures compared to adjacent regions. Therefore, this part of the EAFS may be behaving in a ductile way and allowing creep in the upper crust.

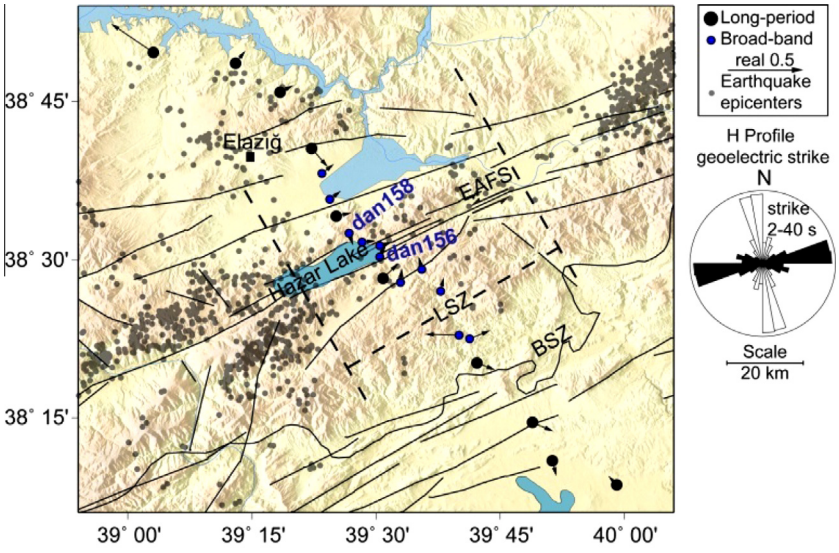

Fig. 2. Magnetotelluric stations used for studies of the East Anatolian Fault System around Hazar Gölü. Small gray dots represent earthquake epicenters from Bulut et al. (2012). Black arrows show real induction vectors averaged over the period range 2–40 s and plotted in the Parkinson convention. Rose diagram show geoelectric strike directions derived from the phase sensitive skew. BSZ: Bitlis Suture Zone; LSZ: Low Seismicity Zone (Dolmaz et al., 2008).

2.3. Previous magnetotelluric studies of the NAF and EAF

Previous studies have shown that MT has the potential to map fluids within major strike-slip faults. A number of MT studies of the North and East Anatolian Fault Systems have been published in recent years. Tank et al. (2005) described the first detailed MT study of the western NAFS (Fig. 1) close to the rupture of the 1999 İzmit earthquake (Barka, 1999). This resistivity structure determined by this MT study showed a zone of low resistivity that was located between the main fault strands, and extending from 10 km depth through the entire crust. Hypocenters of the aftershocks of the İzmit earthquake were located on the southern edge of this low resistivity zone, that was interpreted by Tank et al. (2005) as being caused by a zone with elevated fluid content. This fluid-rich layer just below the seismogenic zone was interpreted as triggering earthquakes and being responsible for post-seismic creep. Kaya et al. (2009) reported two MT profiles crossing the NAF near Düzce that were collected to the west and east of the 1999 Düzce earthquake epicenter. These MT profiles showed higher resistivities on the eastern MT profile, that were interpreted as an explanation for the observed high rupture velocity and aftershock activity on the eastern side of the Düzce fault, compared to the west. Türkoğlu et al. (2008) reported a regional scale MT study of the Arabia–Eurasia collision in Eastern Anatolia (Fig. 1). A widespread low resistivity layer (10–30 Ωm) beneath the Anatolian Plateau was discovered, and interpreted as being due to the presence of a fluid-rich lower crust that was mechanically weak. This layer may well control deformation by (a) permitting crustal flow or (b) locally decoupling of the upper and lower parts of the lithosphere (Türkoğlu et al., 2008). This study also showed that the resistivity in the lithospheric upper mantle beneath the Eastern Anatolian Plateau was 10–30 Ωm, which is an order of magnitude less than expected and could be an indication of a shallow asthenosphere.

Avşar et al. (2012) reported two MT profiles crossing the NAF within the Erzincan Basin (Fig. 1). The western MT profile imaged a DZC spatially correlated with the NAF in the Erzincan basin. The absence of a deeper CFZC under the eastern MT profile was attributed to permeability and fluid content of the NAFS in the Erzincan Basin at shallow depths.

3. Magnetotelluric data collected on the NAFS and EAFS

The survey by Türkoğlu et al. (2008) defined the regional scale resistivity structure of the Arabia–Eurasia collision zone in Eastern Anatolia for the first time. This survey also used more detailed transects to investigate the geoelectric structure of the North and East Anatolian Fault Systems. In each of the two study areas, MT data were collected on profiles that were approximately perpendicular to the surface trace of the faults (denoted as the EAF and NAF profiles). The EAF-profile crosses the EAFS and Bitlis-Zagros Suture Zone (BSZ) close to Hazar Gölü (Fig. 2). This profile consists of 10 long-period and 11 broad-band MT stations (1 broad-band MT station was excluded from the inversions). The NAF profile is located just east of Refahiye (Fig. 3). This profile consists of 9 long-period and 4 broad-band MT stations. The broad-band MT stations typically recorded data for 1–3 days while the long-period MT stations recorded data for 20–30 days. Typically, 3 broadband MT stations and 15 long-period stations were running synchronously and were used for mutual remote reference to remove uncorrelated noise. A quiet station used for the reference that was typically more than 10 km distant from the measurement site. The MT time series data were visually inspected and compared to neighboring stations in order to identify noisy data segments. These were generally caused by electrode problems, broken telluric wires, cultural noise or instrument failure, and were excluded from the processing. The remaining data segments were pre-whitened, Fourier transformed, and estimates of the magnetotelluric impedance were computed using the statistically robust algorithm of Egbert (1997). Smooth MT transfer functions were obtained in the period ranges 0.01–2000 s and 10–10,000 s for broad-band and long-period MT data, respectively. Fig. 4 shows sample MT curves from both the NAF and EAF profiles. A complete set of observed MT data soundings and the computed 2D inversion model responses are shown in the Appendix.

3.1. Dimensionality and directionality of the MT data

The dimensionality of MT data can be investigated in a number of ways. The simple definition of skew proposed by Swift (1967) can be an unreliable way of distinguishing between 2-D and 3-D data if the MT data are affected by galvanic distortion. The phase sensitive skew proposed by Bahr (1991), is relatively insensitive to galvanic distortion effects such as static shifts, and gives a better estimate of the dimensionality than the Swift skew. A skew value greater than 0.3 can be an indication of 3D effects in the data, while a smaller skew value (<0.3) is a necessary, but not sufficient, requirement for the impedance data to be considered 2D (Bahr, 1991). The phase sensitive skew threshold cited above is not statistically defined in terms of noise in the MT impedances, so Marti et al. (2005) introduced the Bahr-Q method. When the MT data are of good quality, Bahr skew and Bahr-Q methods give similar results. The MT data presented in this paper are generally of good quality, so the Bahr skew was used to investigate the dimensionality, as shown in Fig. 5. Overall, the NAF and EAF MT data are characterized by relatively low Bahr skew values (<0.25) over the whole period range. Isolated Bahr skew values (>0.5) are observed at short periods ($T < 10$ s) for the long-period MT stations and are due to noisy or biased data. These data were excluded from subsequent data analysis.

The geoelectric strike direction is needed for subsequent MT data analysis and can be determined using a range of methods

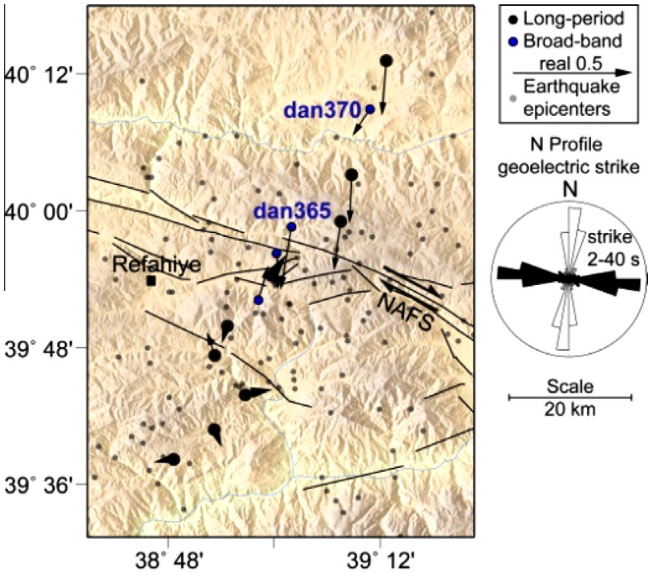

Fig. 3. Magnetotelluric stations used for the study of the North Anatolian Fault System (NAFS) around Refahiye. Small gray dots represent earthquake epicenters from 1960 to 2004 KOERI, Turkelli et al. (2003) and Kaypak and Eyidoğan (2005). Black arrows show real induction vectors averaged over the period range 2–40 s and plotted in the Parkinson convention. Rose diagrams show the geoelectric strike direction derived from the phase sensitive strike.

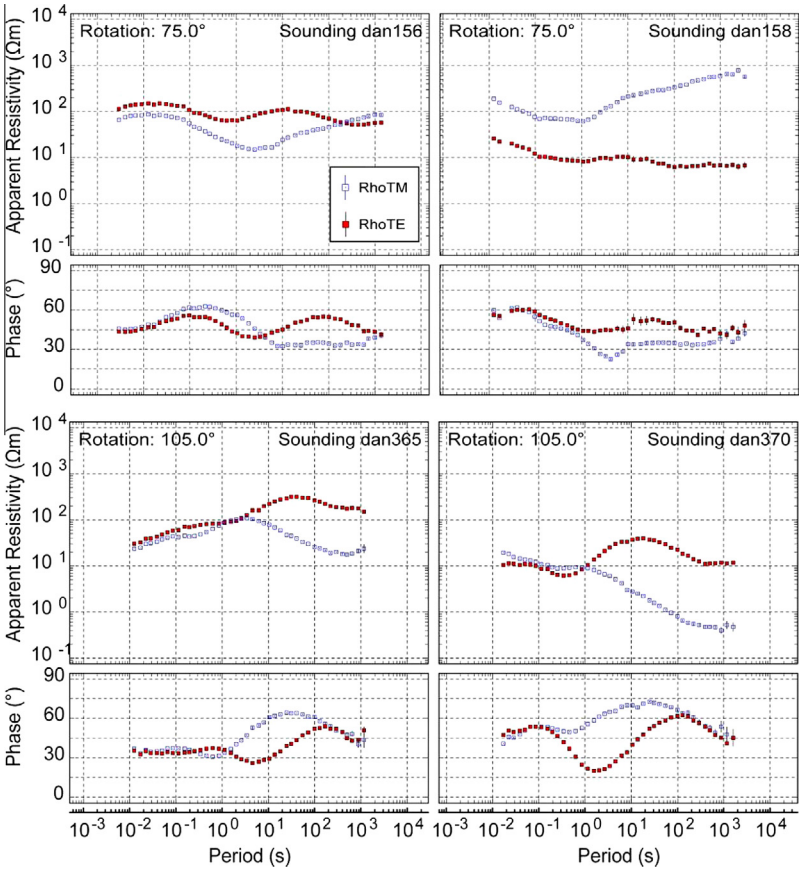

Fig. 4. Apparent resistivity and phase curves for typical MT stations from the NAF (lower row) and EAF-profiles (upper row). Data are shown after rotation to the strike direction. See Figs. 2 and 3 for station locations.

(Simpson and Bahr, 2005). The whole period range was grouped into four period bands to investigate variations of the geoelectric strike direction with increasing period. Note that increasing signal period corresponds to an increasing depth of penetration into the Earth. Phase sensitive strike directions determined from Bahr's (Bahr, 1991) method are shown in Fig. 6. Approximate depth estimates for each of the four period bands were made using the MT skin depth for a range of expected resistivity values based on the apparent resistivity curves and are listed in Fig. 6.

3.1.1. NAF-profile

The short period data ($T < 2$ s) show no well-defined strike direction as the near surface resistivity structure is essentially 1-D and/or has a variable strike direction. The average geoelectric strike direction of the NAF-profile is relatively well defined at N105°E from the first two period bands (2–40 s). This geoelectric strike direction is similar to the strike direction of the NAF as defined by the focal mechanisms of the large earthquakes (Barka and Eyidogan, 1993; Grosser et al., 1998; Aktar et al., 2004) and the strike of the fault trace (Ketin, 1948; Sengör and Kidd, 1979). MT signals with periods greater than 40 s show a well-defined strike direction that is east–west independent of period, and roughly parallel to the Bitlis Suture Zone.

3.1.2. EAF-profile

A similar change in the geoelectric strike direction with period occurs on the EAF-profile (Fig. 6) where a N75°E strike direction changes to east–west at longer periods ($T > 40$ s). The N75°E geoelectric strike direction is close to the N65°–70°E strike of the surface trace of the EAF. Thus for two-dimensional inversions, strike directions of N105°E for the NAF-profile and N75°E for the EAF-profile were used. This choice was made because the target of the survey was the upper crustal structure of the fault, and not the structure at depth sampled by the longer period MT data.

The induction vectors are also plotted on the maps in Figs. 2 and 3. The real part of the induction vectors were averaged over the period range of 2–40 s and plotted in the Parkinson convention with vectors pointing towards conductors. The induction vectors show evidence for a reversal above both the NAFS and EAFS which indicates the fault zones are more conductive than their surroundings. However, the surface trace of the NAFS and the location of the induction vector reversal are not exactly coincident (Fig. 3). On both profiles, the reversals are complicated by other factors, including a significant fault parallel component on the EAFS profile.

3.2. General aspects of the MT data

The observed MT data were rotated to the strike coordinate frames determined above and sample sounding curves are shown in Fig. 4. Typical MT stations on the Arabian Plate show relatively low resistivity values (~10 Ωm) at short periods ($T < 10$ s) and increasing apparent resistivity as the period increases. This behavior could be attributed to a layer of low resistivity sedimentary rocks in the Arabian Foreland overlying the crystalline (resistive) basement rocks of the crust and upper mantle. The MT curves from the Anatolian Block show more spatial variation than those collected on the Arabian Plate. Relatively high apparent resistivities (~100 Ωm) are observed at short periods ($T < 10$ s). Decreasing resistivities are observed at intermediate periods ($10 \text{ s} < T < 1000$ s) and a slight increase of apparent resistivity is

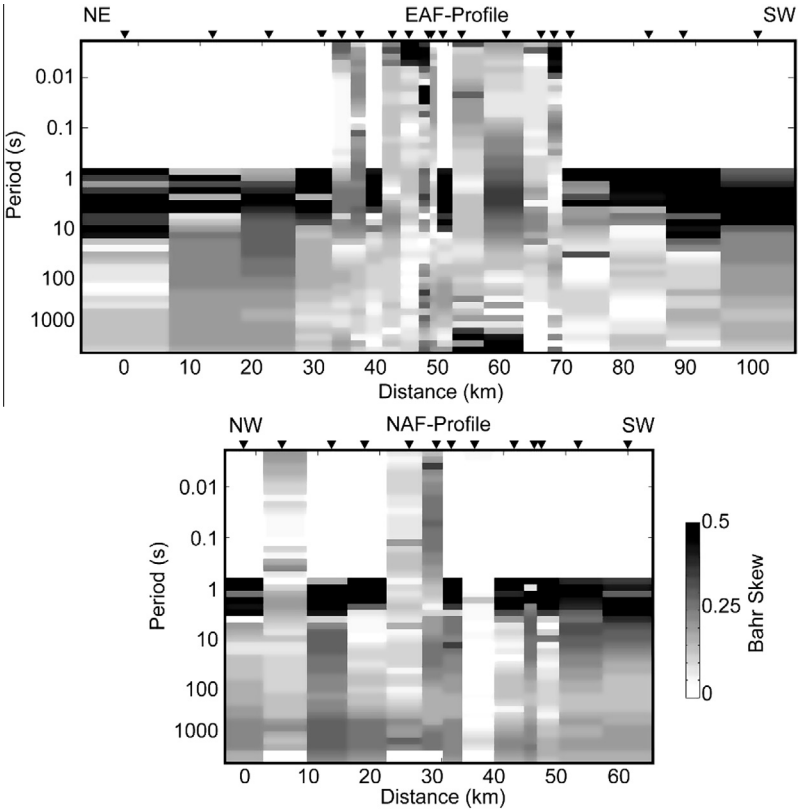

Fig. 5. Bahr's phase sensitive skew (Bahr, 1991) for EAF-profile (top) and NAF-profile (bottom). White space indicates that the data are not available at those particular periods.

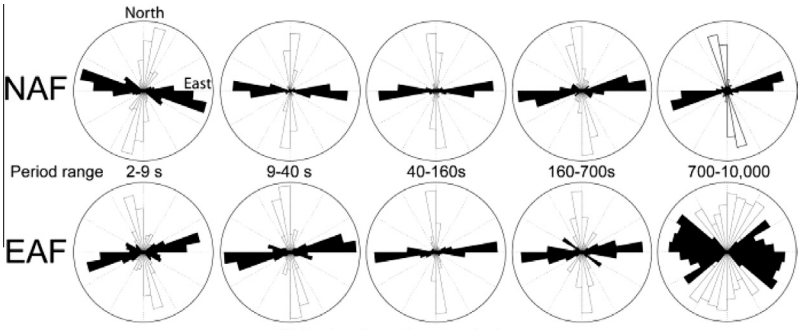

Skin depth estimates in km

Period (s) / Res. (Ωm)	2	9	40	160	700	10,000
10	**2.2**	**4.7**	**10**	**20**	**42**	**159**
100	**7.1**	**15**	**32**	**63**	**133**	**503**

Fig. 6. Bahr's phase sensitive strike direction for four period bands (Bahr, 1991). The MT skin depth equation was used to estimate the approximate depth to which the MT signals penetrate in each period band. Typical apparent resistivities of this data set (10 Ωm and 100 Ωm) were used to estimate the range of skin depths. Rose diagrams represent histogram plots of the strike directions for all the stations. Black and white histograms represent the 90° ambiguity in the strike direction inherent to MT data.

observed at long periods. Qualitative interpretation of the apparent resistivity curves from Anatolian Block typically indicates a low resistivity zone at crustal or sub-crustal depths.

3.3. Two-dimensional MT inversion

The MT stations were projected onto profiles perpendicular to the geoelectric strike directions determined above. Where available, the short period MT data (0.01–10 s) were also included in the inversions to obtain more detailed resistivity models close to the fault zones. The 2-D NLCG algorithm of Rodi and Mackie (2001) was used for inversion of both apparent resistivity and phase for the transverse electric (TE) and transverse magnetic (TM) modes. The vertical magnetic field transfer functions were also inverted. Static shift coefficients were estimated by the inversion algorithm. Error floors of 20%, 5% and 0.02% were assigned for apparent resistivity, phase and tipper data, respectively. Note that 5% in phase is equivalent to 1.43°. The starting model was a homogenous half-space with a resistivity of 100 Ωm with 171 cells in the horizontal direction (∼1 km width) and 111 in the vertical

direction (first cell thickness ~13 m). Initial r.m.s. misfits for the NAF and EAF profiles were 7.87 and 6.36. Identical inversion parameters were used for both the NAF and EAF-profiles.

The final inversion models, static shift coefficients, and r.m.s. misfits obtained after 200 iterations are shown in Fig. 7. It is well known that the MT inverse problem is non-unique (Menke, 1989; Whittall and Oldenburg, 1992) and the solution of the inverse problem requires that additional constraints to be applied to the resistivity model. This is generally achieved with regularization that seeks a resistivity model that minimizes the misfit between the observed and predicted MT data and also keeps the resistivity model as spatially smooth as possible (Tikhonov and Arsenin, 1977). In the NLCG inversion algorithm, the regularization parameter (tau) controls the overall smoothing of the model. As the value of tau increases, the resistivity model becomes smoother and the measured MT data are not fit as well. Fig. 8 shows the trade-off between the MT data fit and resistivity model smoothness. The corner of the so called L-curve defines the optimum value of tau for a given MT data set and a compromise between fitting the MT data and generating a smooth resistivity model. The corner of the L-curve indicates the preferred tau values for this study ranges from tau = 2–10. Relatively large station spacing caused unwanted rough structures between the stations when lower tau values were used. Therefore, a relatively high tau value of 10 was used.

The final inversion models for the NAF and EAF-profiles have r.m.s. misfit values of 1.40 and 1.48, respectively. These values are statistically acceptable and as expected since the dimensionality analysis suggests the impedance tensor is relatively 2-D at most of the MT stations. Static shift coefficients estimated by the inversion were less than half a decade in magnitude at most sites, but there were some sites with higher estimated static shift values (Fig. 7). Static shift coefficient estimation used a damping factor of 10,000 in the initial steps of the inversion process to obtain an optimum fit with the model features, and only allowed static shift coefficients in the later stages of the inversion. Fig. 9 shows the observed and calculated inversion responses as pseudosections for all three data components. Pseudosections show that computed responses from the final inversion model were able to fit all aspects of the observed MT data.

The fit of the inversion response to the observed MT data should be examined to see if a uniform fit is obtained. Ideally a "white" fit

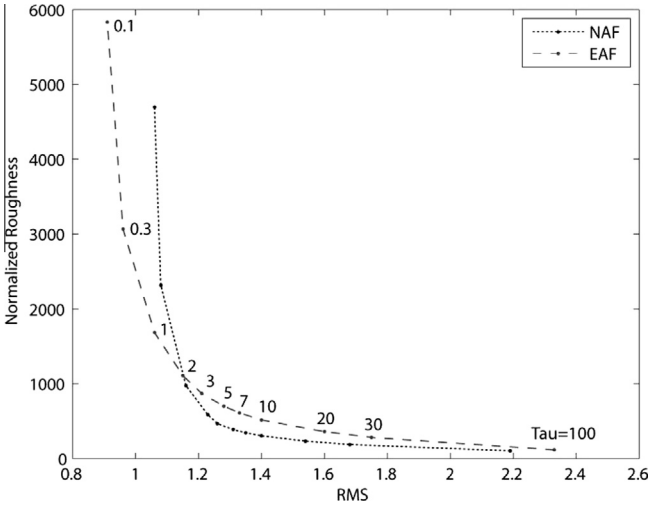

Fig. 8. Resistivity model normalized roughness versus r.m.s. data misfit for a range of tau values for the NAF (dashed line) and EAF (solid line) profiles.

is obtained, with all periods fit equally well. If a particular range of periods are not well fit then the final inversion model may be misleading and smaller error floor values may be needed to focus the inversion on a particular range of periods corresponding to resistivity structures of interest. Fig. 9 shows that a satisfactory fit to the measured data was obtained for the entire period range used for inversion (0.01–10,000 s). Sharp lateral resistivity changes in the pseudo sections occur because computed static shifts have been applied to the apparent resistivities of the model response. In fact, the response data are laterally smoother than they appear in Fig. 9. The data fit is also shown as sounding curves in Figs. SP1 and SP2 for all stations on both profiles.

The inversion model for the EAF-profile shown in Fig. 7 reveals a number of significant features. The EAF represents the main boundary between the resistive block to the south and the low resistivity lower crust (C1) to the north at a distance of around 42 km. This lateral resistivity discontinuity may represent the boundary between the Arabian Plate and the Anatolian Block and appears to dip southeast. Another significant feature of this model is the vertical conductor (C2) located beneath the EAF at a distance

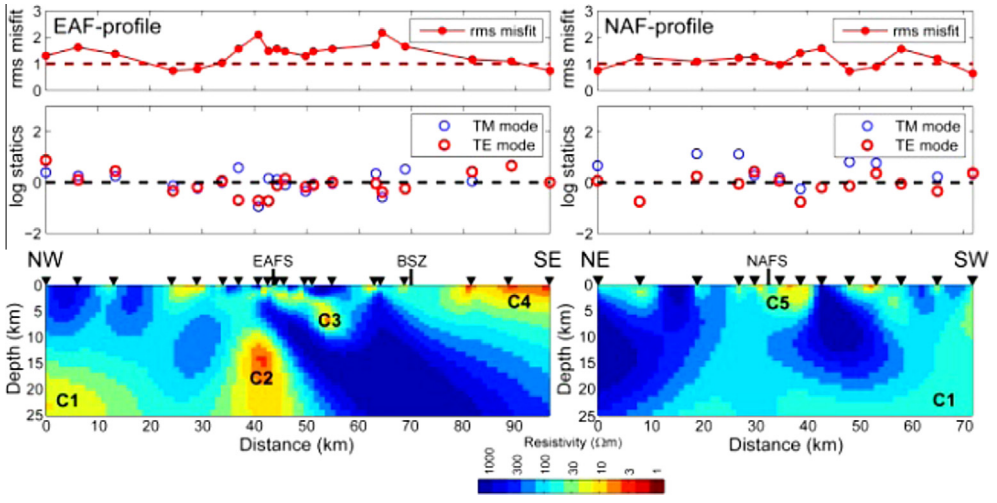

Fig. 7. Upper panels show the r.m.s misfit for 2-D inversions with the following parameters. NAF-profile model used 105° NE strike angle and EAF-profile model used 75° NE; 20%, 5%, 0.02% error floors for apparent resistivity, phase and tipper, respectively; tau = 10. Dashed line shows the preferred r.m.s. misfit value of unity. Middle panels show shift coefficients estimated by the inversion algorithm. The dashed line shows a shift of one which represents no static shift. Lower panels show inversion models for the EAF (left) and NAF (right) profiles.

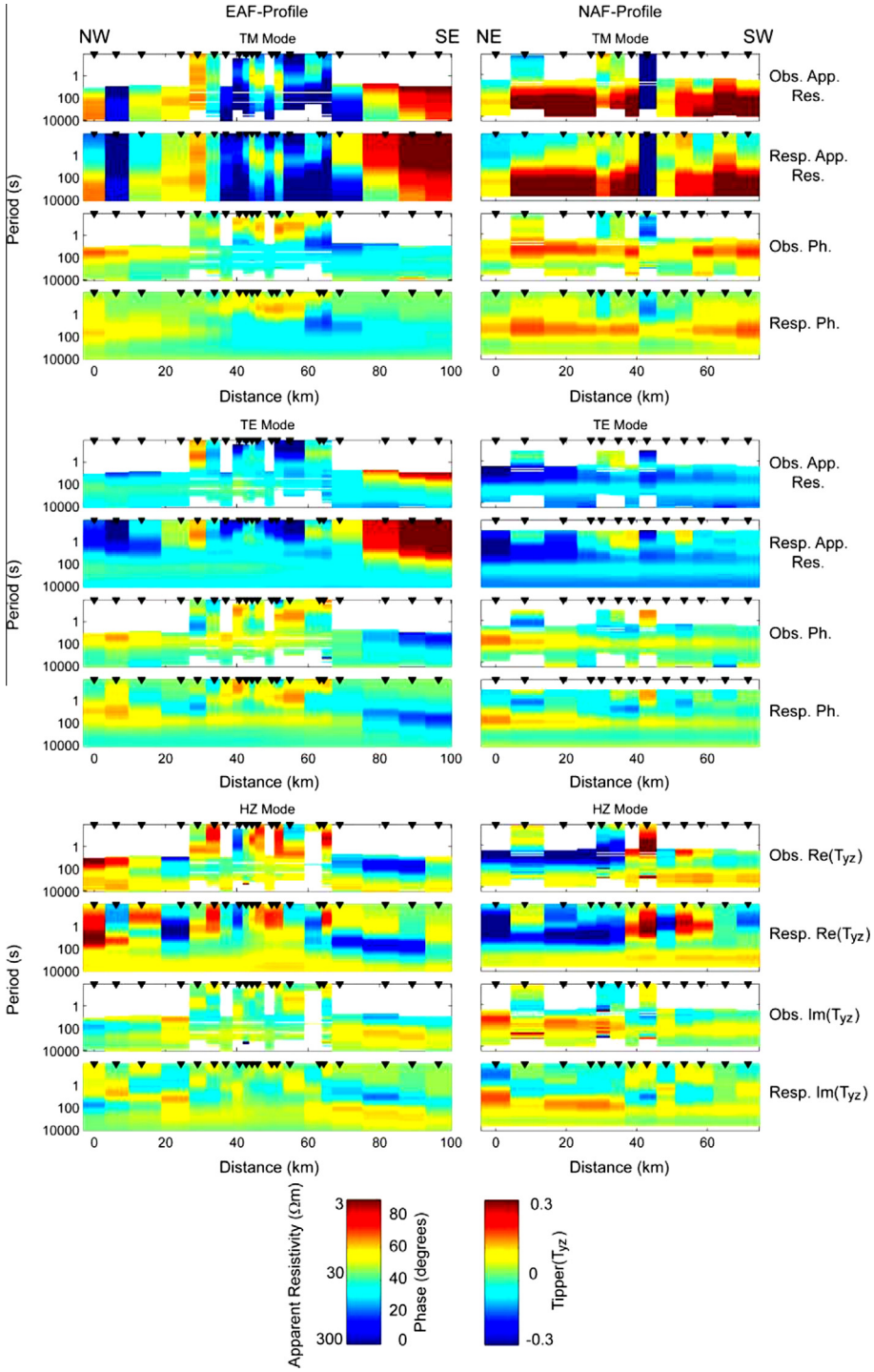

Fig. 9. Pseudosections of the observed data (apparent resistivity, phase and tipper data) and the corresponding responses for the inversion models shown in Fig. 8 for the EAF and NAF-profiles, respectively.

of 45 km with the top at a depth of 10 km, hereafter referred to as the crustal fault zone conductor (CFZC).

The inversion model for the NAF-profile shows a resistive block located south of the surface trace of the NAF and a narrow part of this block reaches the surface. The crustal structure north of the NAFS is highly resistive (>1000 Ωm). In contrast to the resistivity structure of the EAFS, the NAFS is represented by a wider zone of low resistivity but the resistivity beneath the fault zone is one order of magnitude higher than beneath the EAFS.

3.4. Sensitivity of the MT data to the geometry of the CFZC beneath the EAF

The inversion of MT data is a non-unique process and must be understood to determine the degree to which features in the model are required by the MT data. It can be shown that the conductance of a layer can be robustly defined by MT data (conductance is the product of conductivity and thickness). However, when the layer is thin compared to its depth, the thickness and conductivity can-

not be individually resolved. This non-uniqueness can also be partially overcome if a conductive layer is at the surface. When a conductor has a finite horizontal extent, such as the CFZC beneath the EAF, this non-uniqueness can be partially overcome, and more information about the depth variation of conductivity derived from the data. The spatial variation in the vertical magnetic fields are especially useful in this respect, as demonstrated for a near vertical conductor imaged by Bertrand et al. (2009).

To investigate the model resolution, a generic fault zone model was developed, as shown in Fig. 10 and synthetic MT data were calculated and 5% Gaussian noise added. Inversions of the individual MT data components (TE, TM and Hz) do not reveal all features of the original resistivity model. However the joint inversion of TE, TM and Hz reveals all model features, including the CFZC. Note that the CFZC is broader in the inversion model because of the spatial smoothing that is used to regularize the MT inversion and address the non-uniqueness inherent in inversion. Similar model features are observed in both the synthetic inversion models (Fig. 10), and those derived from the field data collected on the EAF profile. This gives support for the presence of a strong CFZC beneath the EAF. The importance of the tipper (Hz) data is no surprise because it is well known that vertical magnetic field data are sensitive to lateral resistivity variations and widely used in mineral exploration for locating discrete conductors. A second set of tests were undertaken to determine if static shifts could have caused the inversion to place a CFZC beneath the EAFS. This was motivated by the observation that three MT stations just north of the EAFS had the largest estimated static shifts on the EAF-profile (Fig. 7) and could have influenced the final resistivity model, and also that the number of the broad band MT stations are limited around the fault zone. The second panel from top in Fig. 11 shows that the presence of a CFZC does not depend on the data at stations dan160, dan159 and dan158 which have high static shift coefficients. The third panel from top in Fig. 11 shows that using only the long period data ($T > 10$ s) is sufficient to recover the CFZC and the other major model features discussed in this paper. The final inversion model without statics found an even more pronounced CFZC and this is expected as the inversion cannot account for model features with static shift coefficients (bottom panel in Fig. 11).

4. Interpretation of resistivity models

4.1. Lower crustal conductor

A lower crustal low resistivity layer (10–30 Ωm) was previously reported at a depth of 20 km throughout Eastern Anatolia by

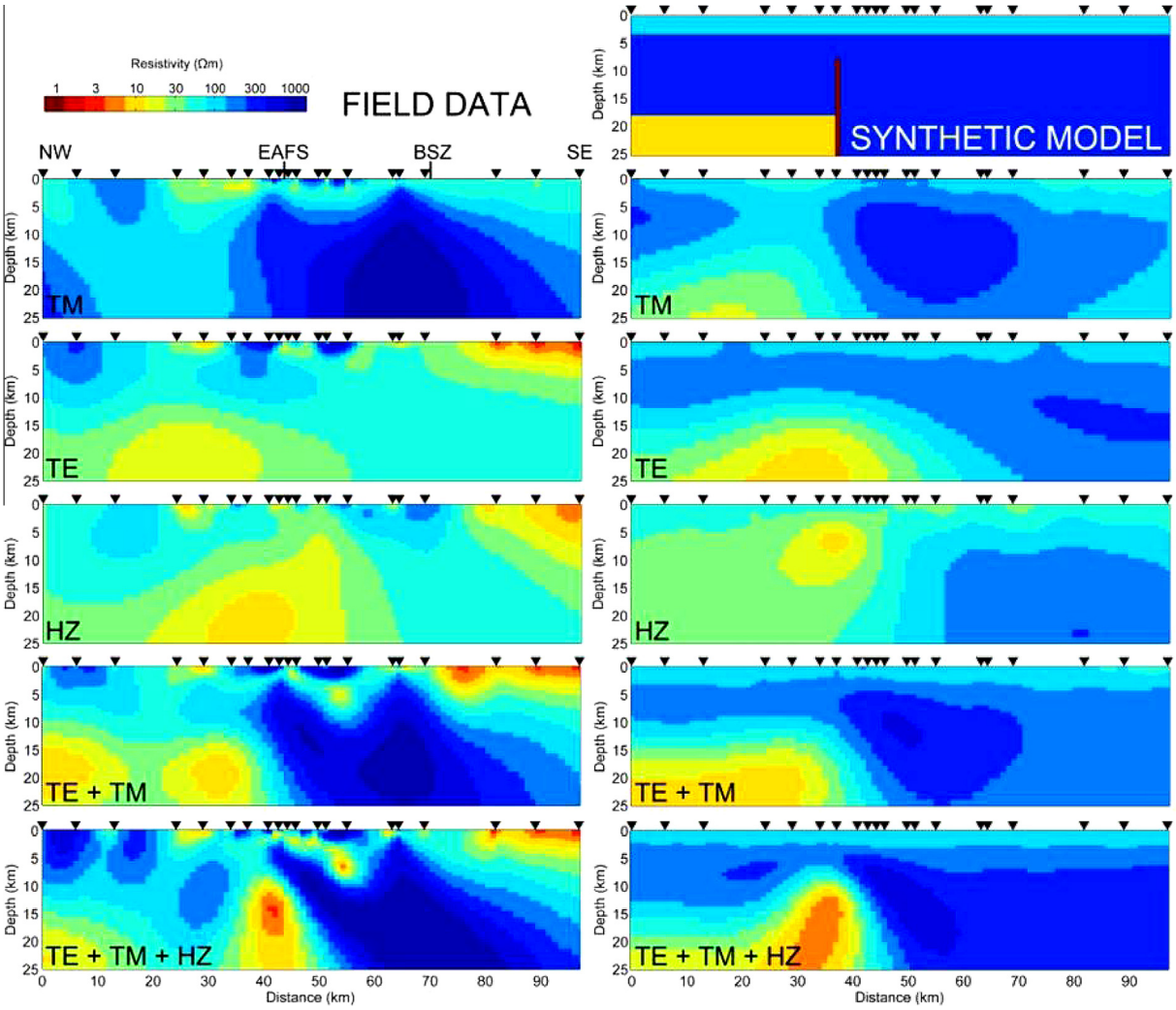

Fig. 10. Left column shows individual and joint inversions of the MT data along the EAF-profile. Right column shows a synthetic experiment to explain the absence of the vertical conductor for individual inversions. The thickness of the vertical conductor was 1 km in the synthetic model. TE + TM inversions start to recover the vertical conductor when the thickness of the conductor is 2 km or thicker (not shown).

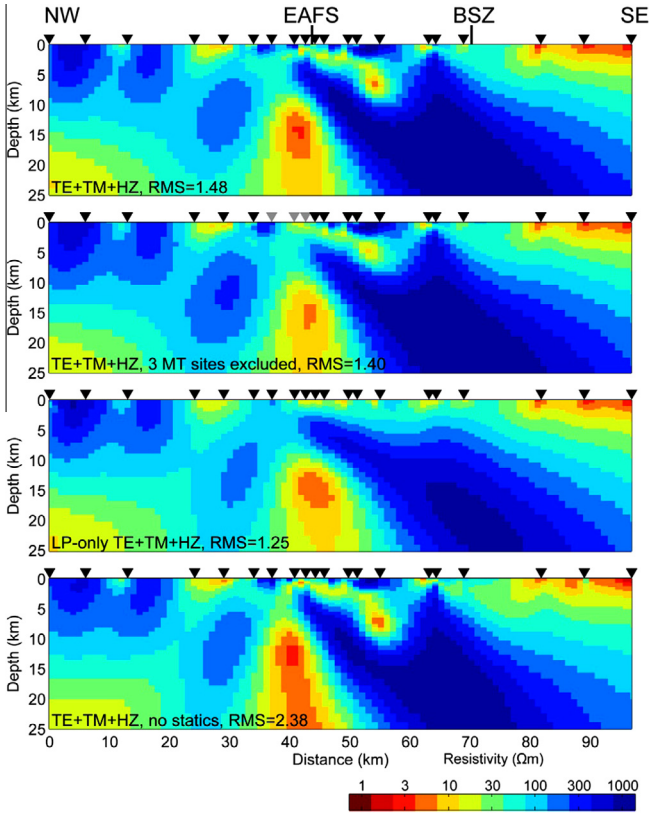

Fig. 11. Inversion experiment to investigate the effect of static shifts on the inversion model for the EAF-profile. From top to bottom; (1) preferred inversion model including all sites and all available periods. Statics shift coefficients were estimated automatically by the inversion, (2) three MT sites with high estimated static shifts excluded, (3) only long-period data ($T > 10$ s) used in the inversion, all sites included, (4) all sites included but the statics are not estimated by the inversion but modeled.

Türkoğlu et al. (2008) who showed that it was bounded on the North and South by the NAF and EAF, respectively. The spatial extent of the layer also coincides with the Eastern Anatolian Accretionary Complex, a low Bouguer gravity anomaly, strong attenuation of S_n waves and low P_n velocities (Ates et al., 1999; Barazangi et al., 2006; Angus et al., 2006; Gök et al., 2007). The low resistivity likely indicates a region of elevated fluid content, most likely partial melt and by inference is a region of weak rheology within the lower crust. While this layer is imaged in the present study (C1), a fuller discussion of its significance is described by Türkoğlu et al. (2008). Of relevance to this study, the layer appears to be connected to the NAF and EAF with a low resistivity vertical feature (Fig. 12).

4.2. Crustal fault zone conductors

The MT profiles described in this paper lack the close station spacing needed to detect a shallow DZC associated with the upper crustal damage zone, such as the conductor discovered on the Central San Andreas Fault. However, the profile geometry is capable of resolving the deeper CFZC that has been observed in the mid-crust beneath a number of strike-slip faults. A conductor of this type is the most prominent feature in the EAF-profile inversion model (C2), and is located beneath the surface trace of the EAF. A weaker feature is associated with the NAF (C5). The geometry and physical properties of these conductors are discussed in the following sections. Fault-zone fluids have been proposed as a mechanism for explaining the apparent low strength of major fault zones (Sleep and Blanpied, 1992) and these fluids lower the bulk resistivity of a rock and can be imaged with magnetotellurics (Unsworth et al., 1997; Unsworth and Bedrosian, 2004).

4.2.1. East Anatolian Fault

The vertically integrated total conductance of the EAFS at Hazar Gölü in the depth range 0–50 km was around 4000 S. The regularization process results in the conductance value being at the lower end of the range consistent with the MT data. The top of the CFZC (feature C2) is at 10 km depth and well constrained by MT data. This is clearly above the depth of the brittle–ductile transition that was defined to be around 20 km by Bektas et al. (2007). A conductance of 4000 S can be explained with many combinations of conductivity and thickness. To give an idea of the range of parameters consistent with the MT data, consider the limit where this feature is thick and extends to the Moho at a depth of 40 km (Zor et al., 2003). In this case the resistivity of C2 should be 7.6 Ωm. In the other limit, C2 is thin and only extends to the brittle–ductile transition zone at a depth of 17–18 km (Bektas et al., 2007) and would have a resistivity of 4.5 Ωm. What fluid content for C2 is implied by a resistivity in the range 7.6–4.5 Ωm? This can be estimated using the empirical Archie's Law (Archie, 1942) that relates the bulk resistivity of the fluid-saturated rock (ρ) to the pore fluid resistivity (ρ_f) and the porosity (ϕ) as $\rho = \rho_f Phi^{-m}$ where m is the cementation factor that describes the spatial distribution of the fluid within the rock, and contains information about permeability. A value of $m = 1$ implies good interconnection with crack shaped pores while $m = 2$ implies poor interconnection with spherical shaped pores. Unsworth and Rondenay (2013) showed that under ambient pressure and temperature, crustal saline fluids typically have a resistivity of in the range 0.01–0.3 Ωm where the range is primarily controlled by the salinity. With $m = 1$, a layer with 7.6 ohm-m layer requires a porosity in the range 0.13–4.0%. If this layer is forced to be thin, with a resistivity of 4.5 Ωm, then a porosity in the range 0.22–6.7% is needed. If $m = 2$ then these ranges become 4.7–26% and 3.6–20% which are unrealistically high. The $m = 1$ porosity values are realistic and reflect the most likely fault zone pore geometry. Reducing the range of porosity values requires additional knowledge of the fluid resistivity, which depends primarily on the salinity.

A surface conductor (C4) is imaged at the southeast end of the EAFS profile and is associated with the sedimentary basin deposited on the Arabian Platform. Another conductor (C3) is also observed dipping southeast away from the surface trace. Detailed geological mapping is not available from this area, so this feature cannot be reliably interpreted but it is likely associated with structures in the sedimentary basin, perhaps formed by fault normal deformation.

4.2.2. North Anatolian Fault

The conductance of the NAFS around Refahiye over the depth range 0–50 km is 1000 S. Using the same approach to calculate the porosity gives a value of 0.1–3% ($m = 1$) for the region of 10 Ωm material extending from the surface to approximately 5 km depth (C5, Fig. 12). In this context it should also be noted that clay minerals are also capable of lowering the electrical resistivity of a fluid bearing rock through the presence of an electrical double layer that forms at the fluid–clay interface which allows ions to move more easily than in the fluid phase. However, it is difficult to distinguish between clay and aqueous fluids on the basis of just the resistivity values imaged with MT data. If Archie's Law is applied, and clay is present, then the porosity derived from Archie's Law will be an upper limit (Worthington, 1993). The clay is also significant because it can lower the friction and modify the seismotectonic behavior of the fault (Hirono et al., 2008).

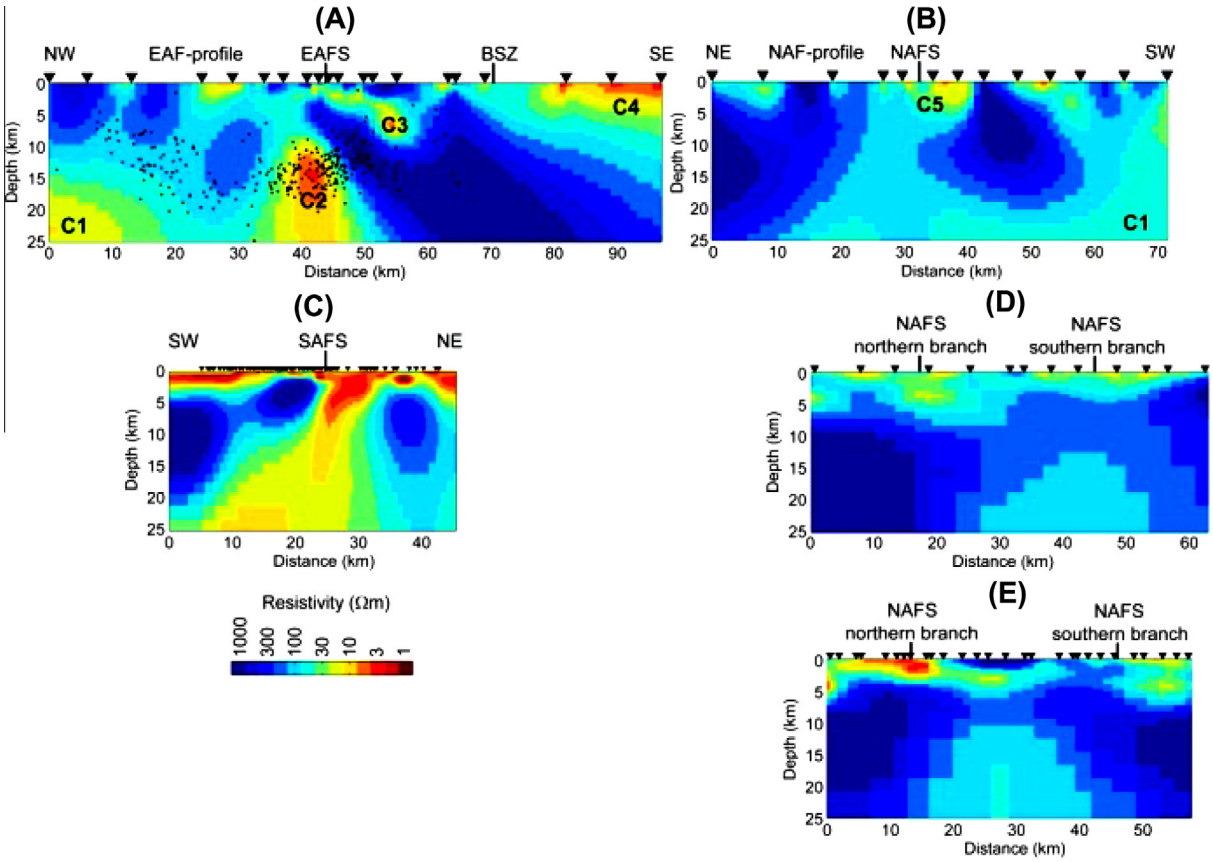

Fig. 12. Resistivity models obtained by 2-D inversion of MT data collected on profiles crossing major strike-slip faults (A) EAF from this study (B) NAF from this study (C) San Andreas Fault at Parkfield from Becken et al. (2008); (D–E) NAF from Tank et al. (2005).

The porosity values estimated for the 0.3 Ωm fluid for the NAF and EAF are comparable to the 8.6% estimated for the San Andreas Fault at Parkfield that assumed a fluid resistivity of 0.3 ohm-m (Unsworth et al., 1997). This is significant because it suggests that despite different source rocks, the fault zone can develop a similar structure.

4.3. Correlation of resistivity structure and seismic behavior

This study has shown that the EAF is characterized by a strong CFZC extending from 10 km to lower crustal depths (C2). The NAF is characterized by a much more subdued conductor (C5). At this point it is important to compare the fault zone resistivity models with those of other fault zones. A key point to consider when making this analysis is that there may be along-strike variations in resistivity structure, which means that a single transect may only be representative a fault segment, rather than the whole fault system. This was found to be the case on the SAFS at Parkfield by Unsworth and Bedrosian (2004).

The station spacing makes it difficult to determine if a shallow DZC conductor is present on the EAF or NAF. A localized DZC a few hundred meters across, such as that observed at Parkfield by Unsworth et al. (1997) would not be detectable with the Eastern Anatolia MT data. However, a CFZC is clearly present beneath the EAF and in Fig. 12 is compared to similar features on other fault zones that have been studied with MT. The resistivity values of the CFZC on the EAF are broadly similar to those observed on the San Andreas Fault at Parkfield (Becken et al., 2008) and Hollister (Bedrosian et al., 2004). However, it should be noted that the DZC and CFZC on the SAF were connected and together extended from the surface to mid-crustal depths, while the CFZC on the EAF begins at 10 km depth. The low resistivity at Parkfield was suggested to be due to aqueous fluids and thus variations in resistivity can be interpreted as indicating regions with elevated concentration of interconnected fluids.

What is the cause of the difference between the structure of the EAFS and the SAFS? One possible explanation is that it is caused by the difference in maturity and accumulated offset of the fault zone.

The EAFS is a relatively immature fault system with 22–33 km offset that developed over the last 2–5 Ma (Şaroğlu et al., 1992; Dewey et al., 1986). It's upper crustal structure is characterized by a number of discrete fault segments around 50 km in length which are aligned approximately parallel to the overall strike of the EAFS (Bulut et al., 2012). The NAF is also relatively young with fault offsets of 75–85 km accumulated over 11–13 Ma (Şengör et al., 2005). In contrast, the central SAF is a more developed, older, mature fault zone with a total offset of 300 km that has accumulated over the last 25 Ma (Revenaugh and Reasoner, 1997) and with a significant amount of deformation localized in a single fault trace.

These differences in maturity and offset could explain the observed differences in resistivity structure between the EAFS/NAFS and the SAF. As a strike-slip fault forms, the strain is localized in the ductile crust, but broadly distributed between a number of discrete faults in the upper crust. This structure was defined in the study area by seismic studies of EAF by Bulut et al. (2012) and in a young transform fault in Walker Lane in the Western United States from geological data by Faulds et al. (2005). As the fault matures, the deformation becomes localized in the upper crust. This temporal development is consistent with the resistivity models derived from the MT data on the EAF. The absence of a low resistivity zone extending to the surface on the EAF is consistent with deformation of a number of discrete brittle faults. The more

mature SAF has upper crustal deformation localized in a narrow zone of fluid filled fractures extending to the surface that produces the observed low resistivity zone.

Another feature to be explained is why this study shows higher resistivity values beneath the NAF than beneath the EAF. The NAF model presented in this paper is similar to that observed further west close to the 1999 ruptures of the İzmit and Düzce earthquakes (Tank et al., 2005). These models also show that the low resistivity region is not connected to the surface. Avşar et al. (2012) published models of the NAF within the Erzincan Basin, but the presence of a low resistivity sedimentary basin prevented effective imaging of the underlying fault zone. The models of the NAF in the Sea of Marmara show a more complex structure that may be due to problems associated with seafloor MT imaging or structural differences such as local extension (Kaya et al., 2013).

Can the hypothesis that fault zone resistivity is controlled by fluid distribution explain the difference in resistivity structure between the NAF and EAF? Both are young strike-slip faults with limited offsets. The resistivity structure of the EAFS implies a higher fluid content at mid-crustal depth than the NAFS – or a higher degree of interconnection. Perhaps the difference is due to differences in the fluid supply. If free fluids are present in the mid and lower crust, they will migrate upwards in the fault zone which is likely a zone of enhanced porosity and permeability. The source of these fluids will depend on the regional tectonics and this could be used to partially explain the variation in CFZC structure in Fig. 12. Both the SAFS and EAFS are located in regions where subduction has occurred in the recent geological past, and introduced fluids into the lower crust and upper mantle. In the EAFS this occurred in the early stages of the Arabia–Eurasia collision. In California, subduction of the Farallon plate occurred prior to the collision of the East Pacific Rise with the trench that led to a plate motion reorganization that formed the modern SAFS (Atwater, 1970). In contrast, the NAFS is further from the locus of subduction and this may have resulted in a drier crust, and resulted in a less pronounced low resistivity within in the fault zone. Additional research is clearly needed to validate this hypothesis.

The analysis above is based on the assumption that the fluid distribution is largely controlled by the style of deformation and fluid supply. An alternate view is that fluid distribution controls the seismicity, and was proposed for the San Andreas Fault where the segments that creep may be associated with an influx of crustal fluids (Irwin and Barnes, 1975). MT profiles on the SAF at Parkfield support the idea that fluid distribution is related to seismicity but cannot separate the cause and effect of crustal fluids and fault behavior. The same problem arises on the NAFS and EAFS in terms of defining correlations between the seismic behavior and resistivity structure, since insufficient geodetic and MT data has been collected to fully define the distribution of creeping – locked segments and associated changes in resistivity structure. Creeping segments have been reported on the western part of the NAFS (Ambraseys, 1970; Aytun, 1982; Çakır et al., 2005) but coincident MT data are not available to constrain the resistivity of the fault zone at these locations. Additional micro-seismic studies are also needed to make this inference. For example, the EAF profile is located in a region where recorded seismic activity on the EAFS is lower than to the east and west (LSZ in Fig. 2) although temporal variations spanning a seismic cycle need to be better defined to address this question.

Finally, it is possible that the stage of the seismic cycle may cause differences in the resistivity structure. The state of stress can control if the fluid-filled fractures in the fault zone are open or closed, and influence the porosity and permeability of the fault zone. The interpretation therefore needs careful consideration of which segment/seismic phase is being sampled by these MT profiles. For example, observations on the North Anatolian Fault may reflect the recent seismic cycle that has ruptured this fault from east to west. In the Elazığ segment of the EAFS investigated in this study may represent a pre-rupture stage with elevated fluid concentrations developing in the fault zone. The origin of the fault zone fluids remains unclear, since trace element, isotopic data and fluid inclusion studies indicate that the source of the water in the fault zone is meteoric or intra-formational (Janssen et al., 1997), rather than a lower crustal or mantle source suggested by Tank et al. (2005) for western NAFS and by Becken et al. (2008) for the SAFS.

4.4. Conclusions

The first MT data collected on the eastern sections of the North Anatolian and East Anatolian Fault Systems are presented in this paper. A zone of relatively low resistivity (100 Ωm) was observed beneath the NAFS around Refahiye and was similar to the upper crustal structure of the western NAFS (Tank et al., 2005). A stronger conductor (CFZC) was detected beneath the EAFS at Hazar Gölü, and was similar to the feature observed beneath the central SAF at Parkfield (Becken et al., 2008). However the top of the EAFS conductor is located at 10 km depth, in contrast to the SAF conductor which begins at the surface and extends through the entire crust. The preferred explanation for this first order difference is the maturity of the two fault systems. The SAFS has developed localized deformation on the central trace, with associated elevated porosity that extends to the surface. In contrast, no such shallow, low resistivity zone exists on the EAFS that is still comprised of discrete faults in the upper crust.

It is not clear if the presence/absence of a CFZC or DZC can be related to the seismic behavior of the fault (locked/creeping). However, it could be that the presence of a CFZC reflects the fluid supply from the mid and lower crust, which may be influenced by episodes of recent subduction. Additional MT, seismic and geodetic studies are needed to determine if the fault zone fluid content is controlling the seismic behavior of these major faults, or whether the fluid distribution is simply a consequence of the deformation.

Acknowledgements

This research was supported by an NSERC Discovery Grant and a grant from the Alberta Ingenuity Fund awarded to Martyn Unsworth, and the Scientific Council of Turkey (TUBITAK). Tuncay Taymaz is thanked for his contributions to many aspects of this project. Volkan Tuncer, Eylem Türkoğlu, Tunç Demir, Ahmet Şener and Bülent Tank are thanked for their help in the field. We are grateful to many Turkish military and government officials and local residents for their help. Phoenix Geophysics are thanked for the loan of an additional MT instrument. Maps were created using GMT software of Wessel and Smith (1991). Alan Jones and Gary McNeice are thanked for providing their tensor decomposition program.

Appendix A. Supplementary data

Supplementary data associated with this article can be found, in the online version, at http://dx.doi.org/10.1016/j.pepi.2015.01.003.

References

Aktar, M., Dorbath, C., Arpat, E., 2004. Seismic velocity and fault structure of Erzincan Basin (Turkey) using local earthquake tomography. Geophys. J. Int. 156, 497–505.

Ambraseys, N., 1970. Some characteristic features of the North Anatolian Fault zone. Tectonophysics 9, 143–165.

Ambraseys, N., 1971. Value of historical records of earthquakes. Nature 232, 375–379.

Ambraseys, N.N., Jackson, J., 1998. Faulting associated with historical and recent earthquakes in the Eastern Mediterranean region. Geophys. J. Int. 133, 390–406.

Angus, D.A., Wilson, D.C., Sandvol, E., Ni, J.F., 2006. Lithospheric structure of the Arabian and Eurasian collision zone in eastern Turkey from S-wave receiver functions. Geophys. J. Int. 166, 1335–1346.

Archie, G.E., 1942. Electrical resistivity log as an aid in determining some reservoir characteristics. Trans. AIME 146, 54–62.

Armijo, R., Meyer, B., Hubert-Ferrari, A., Barka, A., 1999. Westward propagation of North Anatolian Fault into the Northern Aegean: timing and kinematics. Geology 27, 267–270.

Arpat, E., Şaroğlu, F., 1972. The east Anatolian fault system: thoughts on its development. Bull. Miner. Res. Explor. Ins. Turkey 78, 33–39.

Ates, A., Kearey, P., Tufan, S., 1999. New gravity and magnetic anomaly maps of Turkey. Geophys. J. Int. 136, 499–502.

Atwater, T., 1970. Implications of plate tectonics for the Cenozoic tectonic evolution for Western North America. Bull. Geol. Soc. Am. 81, 3513–3536.

Avşar, Ü., Türkoğlu, E., Unsworth, M., Çağlar, İ., Kaypak, B., 2012. Geophysical images of the North Anatolian Fault zone in the Erzincan Basin, eastern Turkey, and their tectonic implications. Pure Appl. Geophys. http://dx.doi.org/10.1007/s00024-012-0521-5.

Aytun, A., 1982. Creep measurements in the Ismetpasa region of the North Anatolian Fault zone. In: Isikara, A.M., Vogel, A. (Eds.), Proceedings Multidisciplinary Approach to Earthquake Prediction. Braunshweig/Wiesbaden, Friedr. Vieweg and Sohn, pp. 279–292.

Bahr, K., 1991. Geological noise in magnetotelluric data: a classification of distortion types. Phys. Earth Planet. Inter. 66, 24–38.

Bai, D., Unsworth, M.J., Meju, M.A., Ma, X., Teng, J., Kong, X., Sun, Y., Sun, J., Wang, L., Jiang, C., Zhao, C., Xiao, P., Liu, M., 2010. Crustal deformation of the eastern Tibetan plateau revealed by magnetotelluric imaging. Nat. Geosci. 3, 358–362.

Barazangi, M., Sandvol, E., Seber, D., 2006. Structure and tectonic evolution of the Anatolian plateau in eastern Turkey. In: Dilek, Y., Pavlides, S. (Eds.), Postcollisional Tectonics and Magmatism in the Mediterranean Region and Asia, vol. 409. Geological Society of America Special Paper, Boulder, Colorado, pp. 463–474.

Barka, A., 1992. The North Anatolian Fault zone. Ann. Tectonicae 6, 164–195.

Barka, A., 1999. The 17 August 1999 İzmit earthquake. Science 285, 1858–1859.

Barka, A.A., Eyidogan, H., 1993. The Erzincan earthquake of 13 March 1992 in eastern Turkey. Terra Nova 5, 190–194.

Barka, A., Kadinsky-Cade, K., 1988. Strike-slip fault geometry in Turkey and its influence on earthquake activity. Tectonics 7, 663–684.

Barka, A., Akyüz, H.S., Altunel, E., Sunal, G., Çakir, Z., Dikbas, A., Yerli, B., Armijo, R., Meyer, B., de Chabalier, J.B., Rockwell, T., Dolan, J.R., Hartleb, R., Dawson, T., Christofferson, S., Tucker, A., Fumal, T., Langridge, R., Stenner, H., Lettis, W., Bachhuber, J., Page, W., 2002. The surface rupture and slip distribution of the 17 August 1999 İzmit earthquake (M 7.4), North Anatolian Fault. Bull. Seismol. Soc. Am. 92 (1), 43–60.

Becken, M., Ritter, O., Park, S.K., Bedrosian, P.A., Weckmann, U., Weber, M., 2008. A deep crustal fluid channel into the San Andreas Fault System near Parkfield, California. Geophys. J. Int. 173 (2), 718–732.

Bedrosian, P.A., Unsworth, M.J., Egbert, G., 2002. Magnetotelluric imaging of the creeping segment of the San Andreas Fault near Hollister. Geophys. Res. Lett. 29. http://dx.doi.org/10.1029/2001GL014119.

Bedrosian, P., Unsworth, M., Egbert, G., Thurber, C., 2004. Geophysical images of the creeping San Andreas Fault: implications for the role of crustal fluids in the earthquake process. Tectonophysics 358, 137–158.

Bektaş, Ö., Ravat, D., Büyüksaraç, A., Bilim, F., Ateş, A., 2007. Regional geothermal characterization of east Anatolia from Aeromagnetic, heat flow and gravity data. Pure Appl. Geophys. 164, 975–998.

Bertrand, E.A., Unsworth, M.J., Chiang, C.W., Chen, C.S., Chen, C.C., Wu, F.T., Türkoğlu, E., Hsu, H.L., Hill, G., 2009. Magnetotelluric evidence for thick skinned tectonics in central Taiwan. Geology 37, 711–714.

Bulut, F., Bohnhoff, M., Eken, T., Janssen, C., Kılıç, T., Dresen, G., 2012. The East Anatolian Fault zone: seismotectonic setting and spatiotemporal characteristics of seismicity based on precise earthquake locations. J. Geophys. Res. 117, B07304. http://dx.doi.org/10.1029/2011JB008966.

Burford, R.O., Harsh, P.W., 1980. Slip on the San Andreas Fault in central California from alignment array surveys. Seismol. Soc. Am. Bull. 70, 1233–1261.

Burke, K., Şengör, C., 1986. Tectonic escape in the evolution of the continental crust. In: Barazangi, M., Brown, L. (Eds.), Reflection Seismology the Continental Crust, vol. 14. AGU Geodyn. Ser., pp. 41–53.

Byerlee, J.D., 1978. Friction of rocks. Pure Appl. Geophys. 116, 615–626.

Byerlee, J., 1993. Model for episodic flow of high pressure water in fault zones before earthquakes. Geology 21, 303–306.

Çakır, Z., Akoglu, A., Belabbes, S., Ergintav, S., Meghraoui, M., 2005. Creeping along the Ismetpasa section of the North Anatolian Fault (western Turkey): Rate and extent from InSAR. Earth Planet. Sci. Lett. 238, 225–234.

Dewey, J.F., Hempton, M.R., Kidd, W.S.F., Şaroğlu, F., Şengor, A.M.C., 1986. Shortening of continental lithosphere: the neotectonics of eastern Anatolia-a young collision zone. In: Coward, M.P., Ries, A.C. (Eds.), Collision Tectonics, vol. 19. Geological Society Special Publication, pp. 3–36.

Dolmaz, M.N., Elitok, Ö., Kalyoncuoglu, Y., 2008. Interpretation of seismicity in the eastern Anatolian collision zone using geophysical (seismicity and aeromagnetic) and geological data. Pure Appl. Geophys. 165, 311–330.

Egbert, G.D., 1997. Robust multiple-station magnetotelluric data processing. Geophys. J. Int. 130, 475–496.

Evans, K.F., Burford, R.O., King, G.C.P., 1981. Propagating episodic creep and aseismic behavior of the Calaveras Fault north of Hollister, California. J. Geophys. Res. 86, 3721–3735.

Faulds, J.E., Henry, C.D., Hinz, N.H., 2005. Kinematics of the northern Walker lane: an incipient transform fault along the Pacific-North American plate boundary. Geology 33 (6), 505–508.

Fuenzalida, H., Dorbath, L., Cisternas, A., Eyidoğan, H., Barka, A.A., Rivera, L., Haessler, H., Philip, H., Lyberis, N., 1997. Mechanism of the 1992 Erzincan earthquake and its aftershocks, tectonics of the Erzincan Basin and decoupling of the North Anatolian Fault. Geophys. J. Int. 129, 1–28.

Gök, R., Pasyanos, M., Zor, E., 2007. Lithospheric structure of the continent-continent collision zone: eastern Turkey. Geophys. J. Int. 169, 1079–1088.

Grosser, H., Baumbach, M., Berckhemer, H., Baier, B., Karahan, A., Schelle, H., Kruger, F., Paulat, A., Michel, G., Demirtas, R., Gençoğlu, S., Yılmaz, R., 1998. The Erzincan (Turkey) earthquake (M_S = 6. 8) of March 13, 1992 and its aftershock sequence. Pure Appl. Geophys. 152, 465–505.

Hanmer, S., 1988. Great Slave Lake shear zone, Canadian Shield: reconstructed vertical profile of a crustal-scale fault zone. Tectonophysics 149, 245–264.

Hempton, M.R., 1985. Structure and morphology of the east Anatolian transform fault zone near Lake Hazar, southeastern Turkey. Geol. Soc. Am. Bull. 96, 233–243.

Hirono, T., Fujimoto, K., Yokoyama, T., Hamada, Y., Tanikawa, W., Tadai, O., Mishima, T., Tanimizu, M., Lin, W., Soh, W., Song, S.R., 2008. Clay mineral reactions caused by frictional heating during an earthquake: an example from the Taiwan Chelungpu fault. Geophys. Res. Lett. 35, L16303.

Irwin, W.P., Barnes, I., 1975. Effect of geologic structure and metamorphic fluids on seismic behavior of the San Andreas fault system in central and northern California. Geology 3, 713–716.

Jackson, J., McKenzie, D., 1988. The relationship between plate motions and seismic moment tensors and the rate of active deformation in the Mediterranean and Middle East. Geophys. J. R. Astronomical Soc. 93, 45–73.

Janssen, C., Michel, G.W., Bau, M., Luders, V., Muhle, K., 1997. The North Anatolian Fault zone and the role of fluids in seismogenic deformation. J. Geol. 105, 387–403.

Karabacak, V., Altunel, E., Cakir, Z., 2011. Monitoring aseismic surface creep along the North Anatolian Fault (Turkey) using ground-based LIDAR. Earth Planet. Sci. Lett. 304, 64–70.

Kaya, T., Tank, S.B., Tunçer, M.K., Rokoityansky, I.R., Tolak, E., Savchenko, T., 2009. Asperity along the North Anatolian Fault imaged by magnetotellurics at Düzce, Turkey. Earth Planets Space 61, 871–884.

Kaya, T., Kasaya, T., Tank, S.B., Ogawa, Y., Tuncer, M.K., Oshiman, N., Honkura, Y., Matsushima, M., 2013. Electrical characterization of the North Anatolian Fault zone underneath the Marmara Sea, Turkey by ocean bottom magnetotellurics. Geophys. J. Int. 193 (2), 664–677.

Kaypak, B., Eyidoğan, H., 2005. One dimensional crustal structure of the Erzincan Basin, eastern Turkey and relocations of the 1992 Erzincan earthquake (M_S = 6.8) aftershock sequence. Phys. Earth Planet. Sci. 151, 1–20.

Ketin, İ., 1948. Über die tektonisch-mechanischen Folgerungen aus den grossen anatolischen Erdbeben des letzten Dezenniums. Geol. Rund. 36, 77–83.

King, G.C.P., Hubert-Ferrari, A., Nalbant, S.S., Meyer, B., Armijo, R., Bowman, D., 2001. Coulomb interactions and the 17 August 1999 İzmit, Turkey earthquake. C.R. Acad. Sci. II Ser. A 333, 557–569.

Kutoglu, H.S., Akcın, H., 2006. Determination of the 30-year creep trend on the Ismetpasa segment of the North Anatolian Fault using an old geodetic network. Earth Planets Space 58 (8), 937–942.

Le Pape, F., Jones, A.G., Vozar, J., Wei, W., 2012. Penetration of crustal melt beyond the Kunlun Fault in Northern Tibet. Nat. Geosci. 5, 330–335.

Le Pichon, X., Şengör, A.M.C., Demirbağ, E., Rangin, C., İmren, C., Armijo, R., Görür, N., Çağatay, N., Mercier de Lepinay, B., Meyer, B., Saatçılar, R., Tok, B., 2001. The active Main Marmara Fault. Earth Planet. Sci. Lett. 192, 595–616.

Le Pichon, X., Chamot-Rooke, N., Rangin, C., Şengör, A.M.C., 2003. The North Anatolian Fault in the Sea of Marmara. J. Geophys. Res. 108, 2179.

Mackie, R.L., Livelybrooks, D.W., Madden, T.R., Larsen, J.C., 1997. A magnetotelluric investigation of the San Andreas Fault at Carrizo Plain, California. Geophys. Res. Lett. 24, 1847–1850.

Marti, A., Queralt, Q., Jones, A.G., Ledo, J., 2005. Improving Bahr's invariant parameters using the WAL approach. Geophys. J. Int. 163, 38–41.

Menke, W., 1989. Geophysical data analysis: discrete inverse theory. Int. Geophys. Ser. 45.

Mount, V.S., Suppe, J., 1987. State of stress near the San Andreas Fault: implications for wrench tectonics. Geology 15, 1143–1146.

Nalbant, S.S., McCloskey, J., Steacy, S., Barka, A.A., 2002. Stress accumulation and increased seismic risk in eastern Turkey. Earth Planet. Sci. Lett. 195, 291–298.

Parsons, T., Toda, S., Stein, R.S., Barka, A., Dietrich, J.H., 2000. Heightened odds of large earthquakes near İstanbul: an interaction based probability calculation. Science 288, 661–665.

Provost, A.S., Chery, J., Hassani, R., 2003. 3-D mechanical modeling of the GPS velocity field along the North Anatolian Fault. Earth Planet. Sci. Lett. 209, 361–377.

Reilinger, R., McClusky, S., Vernant, P., Lawrence, S., Ergintav, S., Cakmak, R., Ozener, H., Kadirov, F., Guliev, I., Ruben, S., Nadariya, M., Hahubia, G., Mahmoud, S., Sakr, K., ArRajehi, A., Paradissis, D., Al-Aydrus, A., Prilepin, M., Guseva, T., Evren, E., Dmitrotsa, A., Filikov, S.V., Gomez, F., Al-Ghazzi, R., Karam, G., 2006. GPS constraints on continental deformation in the Africa–Arabia–Eurasia

continental collision zone and implications for the dynamics of plate interactions. J. Geophys. Res. 111, B05411. http://dx.doi.org/10.1029/2005JB004051.
Revenaugh, J., Reasoner, C., 1997. Cumulative offset of the San Andreas Fault in central California: a seismic approach. Geology 25, 123–126.
Rodi, W., Mackie, R.L., 2001. Nonlinear conjugate gradients algorithm for 2-D magnetotelluric inversions. Geophysics 66, 174–187.
Şaroğlu, F., Emre, Ö., Kuşçu, İ., 1992. Türkiye Diri Fay Haritası (Active Fault Map of Turkey), Scale 1:2,000,000, One Sheet. Ankara, Maden Tetk. Arama Genel Müdürlüğü.
Şengör, A.M.C., Kidd, W.S.F., 1979. Post-collisional tectonics of the Turkish-Iranian Plateau and a comparison with Tibet. Tectonophysics 55, 361–376.
Şengör, A.M.C., Görür, N., Şaroğlu, F., 1985. Strikeslip faulting and related basin formation in zones of tectonic escape Turkey as a case study. In: Biddle, K.T., Christie-Blick, K. (Eds.), Strike-slip Deformation Basin Formation and Sedimentation, vol. 37. Soc. Econ. Paleontol. Miner. Spec. Publ., pp. 227–264.
Şengör, A.M.C., Tüysüz, O., İmren, C., Sakınç, M., Eyidoğan, H., Görür, N., Le Pichon, X., Rangin, C., 2005. The North Anatolian Fault: a new look. Annu. Rev. Earth Planet. Sci. 33, 37–112.
Sibson, R.H., 1974. Frictional constraints on thrust, wrench and normal faults. Nature 249, 542–544.
Sibson, R.H., 1977. Fault rocks and fault mechanisms. J. Geol. Soc. London 133, 191–214.
Simpson, F., Bahr, K., 2005. Practical Magnetotellurics. Cambridge University Press, p. 254.
Sleep, N.H., Blanpied, M.L., 1992. Creep, compaction and the weak rheology of major faults. Nature 359, 687–692.
Stein, R.S., Barka, A., Dieterich, J.H., 1997. Progressive failure on the North Anatolian Fault since 1939 by earthquake stress triggering. Geophys. J. Int. 128, 594–604.
Swift, C.M., 1967. A Magnetotelluric Investigation of an Electrical Conductivity Anomaly in the Southwestern United States (Ph.D. thesis). Mass. Inst. of Tech.
Tank, S.B., Honkura, Y., Ogawa, Y., Matsushima, M., Oshiman, N., Tuncer, M.K., Celik, C., Tolak, E., Işıkara, A.M., 2005. Magnetotelluric imaging of the Fault Rupture area of the 1999 İzmit (Turkey) earthquake. Phys. Earth Planet. Inter. 150, 213–225.
Taymaz, T., Eyidoğan, H., Jackson, J., 2007. Source parameters of large earthquakes in the East Anatolian Fault Zone (Turkey). Geophys. J. Int. 106, 537–550.
Tikhonov, A.N., Arsenin, V.Y., 1977. Solutions of Ill-Posed Problems. V.H. Winston and Sons, Washington, D.C..
Toppozada, T.R., Branum, D., 2002. California M ⩾ 5.5 earthquakes, history and areas damaged. In: Lee, W.H., Kanamori, H., Jennings, P. (Eds.), International Handbook of Earthquake and Engineering Seismology. International Association of Seismology and Physics of the Earth's Interior.
Tullis, J., Yund, R., Farver, J., 1996. Deformation-enhanced fluid distribution in feldspar aggregates and implications for double shear zones. Geology 24, 63–66.
Turkelli, N., Sandvol, E., Zor, E., Gök, R., Bekler, T., Al-Lazki, A., Karabulut, H., Kuleli, S., Eken, T., Gürbüz, C., Bayraktutan, S., Seber, D., Barazangi, M., 2003. Seismogenic zones in Eastern Turkey. Geophys. Res. Lett. 30 (24), 8039.
Türkoğlu, E., Unsworth, M., Çağlar, İ., Tuncer, V., Avşar, Ü., 2008. Lithospheric structure of the Arabia–Eurasia collision zone in eastern Anatolia: magnetotelluric evidence for widespread weakening by fluids? Geology 36, 619–622.
Unsworth, M.J., Bedrosian, P., 2004. Electrical resistivity structure at the SAFOD site from magnetotelluric exploration. Geophys. Res. Lett. 31, L12S05, http://dx.doi.org/10.1029/2003GL019405.
Unsworth, M.J., Malin, P.E., Egbert, G.D., Booker, J.R., 1997. Internal structure of the San Andreas Fault zone at Parkfield. Calif. Geol. 25, 359–362.
Unsworth, M.J., Egbert, G.D., Booker, J.R., 1999. High resolution electromagnetic imaging of the San Andreas Fault in central California. J. Geophys. Res. 104, 1131–1150.
Unsworth, M.J., Wei, W., Jones, A.G., Li, S., Bedrosian, P.A., Booker, J.R., Jin, S., Deng, M., 2004. Crustal and upper mantle structure of Northern Tibet imaged with magnetotelluric data. J. Geophys. Res. 109. http://dx.doi.org/10.1029/2002JB002305.
Unsworth, M.J., Rondenay, S., 2013. Mapping the distribution of fluids in the crust and lithospheric mantle utilizing geophysical methods. In: Harlov, D.E., Austrheim, H. (Eds.), Metasomatism and Metamorphism: The Role of Fluids in Crustal and Upper Mantle Processes. Springer-Verlag, Berlin Heidelberg, pp. 535–598. http://dx.doi.org/10.1007/978-3-642-28394-9_13 (Chapter 13), Lectures in Earth Sciences.
Vozoff, K., 1991. The magnetotelluric method. In: Nabighian, Misac N. (Ed.), Electromagnetic Methods in Applied Geophysics, vol. 2. SEG, pp. 641–711.
Wannamaker, P.E., Jiracek, G.R., Stodt, J.A., Caldwell, T.G., Gonzalez, V.M., Mcknight, J.D., Porter, A.D., 2002. Fluid generation and pathways beneath an active compressional orogen, the New Zealand Southern Alps, inferred from magnetotelluric data. J. Geophys. Res. 107, 1–21.
Wessel, P., Smith, W., 1991. Free software helps map and display data. EOS Trans. Am. Geophys. Union 72, 445–446.
Whittall, K.P. Oldenburg, D.W., 1992. Inversion of Magnetotelluric Data for a One Dimensional Conductivity, Society of Exploration Geophysics monograph. 5.
Williams, C.F., Grubb, F.V., Galanis Jr., S.P., 2004. Heat flow in the SAFOD pilot hole and implications for the strength of the San Andreas Fault. Geophys. Res. Lett. 31.
Worthington, P.F., 1993. The uses and abuses of the Archie equations, 1: the formation factor–porosity relationship. J. Appl. Geophys. 30, 215–228.
Zhang, L., Unsworth, M.J., Jones, A.G., Le Pape, F., Vozar, J., 2015. Lithospheric electrical structure across the Eastern Segment of the Altyn Tagh Fault on the Northern Margin of the Tibetan Plateau. Acta Geol. Sinica (in press).
Zoback, M.D., Zoback, M.L., Mount, V.S., Suppe, J., Eaton, J.P., Healy, J.H., Oppenheimer, D., Reasenberg, P., Jones, L.M., Raleigh, C.B., Wong, I.G., Scotti, O., Wentworth, C., 1987. New evidence on the state of stress of the San Andreas Fault system. Science 238, 1105–1111.
Zor, E., Gürbüz, C., Türkelli, N., Sandvol, E., Seber, D., Barazangi, M., 2003. The crustal structure of the East Anatolian Plateau from receiver functions. Geophys. Res. Lett. 30 (24), 8044.